Efficient Perovskite Hybrid Photovoltaics via Alcohol-Vapor Annealing Treatment

Chang Liu, Kai Wang, Chao Yi, Xiaojun Shi, Adam W. Smith, Xiong Gong, and Alan J. Heeger*

In this work, alcohol-vapor solvent annealing treatment on $CH_3NH_3PbI_3$ thin films is reported, aiming to improve the crystal growth and increase the grain size of the $CH_3NH_3PbI_3$ crystal, thus boosting the performance of perovskite photovoltaics. By selectively controlling the CH_3NH_3I precursor, larger-grain size, higher crystallinity, and pinhole-free $CH_3NH_3PbI_3$ thin films are realized, which result in enhanced charge carrier diffusion length, decreased charge carrier recombination, and suppressed dark currents. As a result, over 43% enhanced efficiency along with high reproducibility and eliminated photocurrent hysteresis behavior are observed from perovskite hybrid solar cells (pero-HSCs) where the $CH_3NH_3PbI_3$ thin films are treated by methanol vapor as compared with that of pristine pero-HSCs where the $CH_3NH_3PbI_3$ thin films are without any alcohol vapor treatment. In addition, the dramatically restrained dark currents and raised photocurrents give rise to over ten times enhanced detectivities for perovskite hybrid photodetectors, reaching over 10^{13} cm $Hz^{1/2}$ W^{-1} (Jones) from 375 to 800 nm. These results demonstrate that the method provides a simple and facile way to boost the device performance of perovskite photovoltaics.

1. Introduction

Methylammonium lead halide perovskites ($CH_3NH_3PbI_3$) have been intensively investigated as the light absorbers for high performance photovoltaics (PVs)[1–11] including efficient perovskite hybrid solar cells (pero-HSCs)[12–14] and ultrasensitive perovskite hybrid photodetectors (pero-HPDs),[7–11] owing to their large absorption coefficient and weakly bounded excitons with long charge diffusion length (≈100 nm).[15,16] However, the large deviations of power conversion efficiencies (PCEs) originated from the randomly formed and distributed $CH_3NH_3PbI_3$ crystals, and the photocurrent hysteresis behavior induced by the defect-assisted trapping in the $CH_3NH_3PbI_3$ crystals,[17,18] have been demonstrated to be the major obstructions to the commercial viability of pero-HSCs. Moreover, the defects in the $CH_3NH_3PbI_3$ crystals provide current leakage pathways, which raises the dark current and deteriorates the photodetectivity of pero-HPDs.[8] To circumvent above deficiencies, great efforts, such as thermal annealing,[19] vapor assisted perovskite formation,[20] solvent additives,[21,22] and mixed solvents for perovskite precursors,[23,24] have been paid to reduce the defects in the $CH_3NH_3PbI_3$ thin films and increase the crystallinity and grain size of the $CH_3NH_3PbI_3$ crystals. Among them, solvent vapor annealing[25] was demonstrated to be one of the most effective and facile ways to improve the crystal morphology of $CH_3NH_3PbI_3$.

Recently, Huang and co-workers found that both the crystallinity and grain size are enhanced by introducing the solvent vapor *N,N*-dimethylformamide (DMF) during the processes of PbI_2 reacted with CH_3NH_3I and the crystal growth of $CH_3NH_3PbI_3$, resulting in suppressed defects-assisted traps and thus enhanced performance of pero-HSCs.[25] The origin of the delightful consequence is probably the retarded crystal formation of $CH_3NH_3PbI_3$ thanks to the good solubility of PbI_2 and CH_3NH_3I in DMF, which leads to the formation of a preferable state of the $CH_3NH_3PbI_3$ grains. It is also noted that to form a dense and compact PbI_2 is of critical importance for ensuring a pinhole-free perovskite thin film, which stimulates the great efforts being dedicated in improving the film morphology of PbI_2 layer through solvent engineering during the PbI_2 crystallization process.[26–28] However, DMF solvent, introduced into the PbI_2-CH_3NH_3I system during the perovskite reaction, would firstly dissolve PbI_2 and then induce the recrystallization process of $CH_3NH_3PbI_3$.[25] And this process could compromise the PbI_2 dense film and generate pinholes if the concentration of DMF vapor and the recrystallization rate were not precisely controlled.

In this scenario, we apply three different alcohols: methanol, ethanol, and isopropanol, in which CH_3NH_3I rather than PbI_2 possess a good solubility, as the solvent vapors to selectively control the dynamic transitions of CH_3NH_3I, leaving the PbI_2 layer as a dense film to ensure a pinhole-free perovskite layer. CH_3NH_3I can easily diffuse into the PbI_2 film due to its highly

C. Liu, K. Wang, C. Yi, Prof. X. Gong
Department of Polymer Engineering
The University of Akron
Akron, OH 44325, USA
E-mail: xgong@uakron.edu
X. Shi, Prof. A. W. Smith
Department of Chemistry
The University of Akron
Akron, OH 44325, USA
Prof. A. J. Heeger
Center for Polymers and Organic Solids
University of California
Santa Barbara, CA 931006, USA

DOI: 10.1002/adfm.201504041

kinetic reactivity, which would facilitate PbI_2 fully reacted with CH_3NH_3I precursors to generate $CH_3NH_3PbI_3$. In addition, CH_3NH_3I is more volatile than PbI_2 during the thermal annealing process, which leads to the deficiency of CH_3NH_3I and leaves the redundant PbI_2 as the insulating components in the perovskite thin film. Therefore introducing a solvent, in which CH_3NH_3I has a good solubility, during the process of the crystal formation of $CH_3NH_3PbI_3$, would effectively facilitate the intercalation of CH_3NH_3I into PbI_2 crystals for fully reaction, as well as elongating the crystal growth of $CH_3NH_3PbI_3$ for pinhole-free thin films. By using above three alcohol solvents to treat the $CH_3NH_3PbI_3$ thin films, we find the increased crystallinity and grain size of $CH_3NH_3PbI_3$ crystals, resulting in enhanced charge carrier diffusion length, decreased charge carrier recombination, and suppressed dark currents in perovskite PVs (pero-PVs). It is also found that different polarities of these three alcohols impose different effects on the $CH_3NH_3PbI_3$ crystal formation. The investigations of the $CH_3NH_3PbI_3$ thin films by grazing incident wide-angle X-ray (GIWAX) diffraction, time-resolved photoluminescence (PL), and scanning electron microscope (SEM) reveal that the $CH_3NH_3PbI_3$ thin film possess high ordered crystals with larger sizes and less defects when it is treated by alcohol solvents with high polarity. As a result, over 43% enhanced PCE along with high reproducibility and eliminated hysteresis behaviors are obtained from the pero-HSCs where the $CH_3NH_3PbI_3$ thin films are treated by methanol vapor as compared with that of pristine pero-HSCs where the $CH_3NH_3PbI_3$ thin films are without any alcohol vapor treatment. In addition, the dramatically restrained dark currents, attributed to the reduced defects in the $CH_3NH_3PbI_3$ crystals, combined with the augmented photocurrent, give rise to over ten times enhanced detectivities for the pero-HPDs, reaching over 10^{13} cm $Hz^{1/2}$ W^{-1} (Jones) from 375 to 800 nm.

2. Results and Discussion

Since CH_3NH_3I, rather than PbI_2, possesses a good solubility in methanol, ethanol, and isopropanol, these alcohols are chosen for treating the $CH_3NH_3PbI_3$ thin films, which would facilitate the intercalation of CH_3NH_3I into PbI_2 crystals for fully reaction, as well as elongating the crystal growth of $CH_3NH_3PbI_3$ for pinhole-free thin films.[29] As a result, enlarged charge carrier diffusion length, decreased charge carrier recombination, and suppressed dark currents are expected, giving rise to improved performance pero-HSCs and pero-HPDs.[30,31] In order to verify these hypothesis, the influence of the alcohol-vapor annealing treatment on the $CH_3NH_3PbI_3$ crystals is firstly investigated. The experimental procedures of the alcohol-vapor annealing treatment on the $CH_3NH_3PbI_3$ layer are illustrated in **Scheme 1**. The $CH_3NH_3PbI_3$ films are fabricated by the interdiffusion of PbI_2 and CH_3NH_3I double layers as

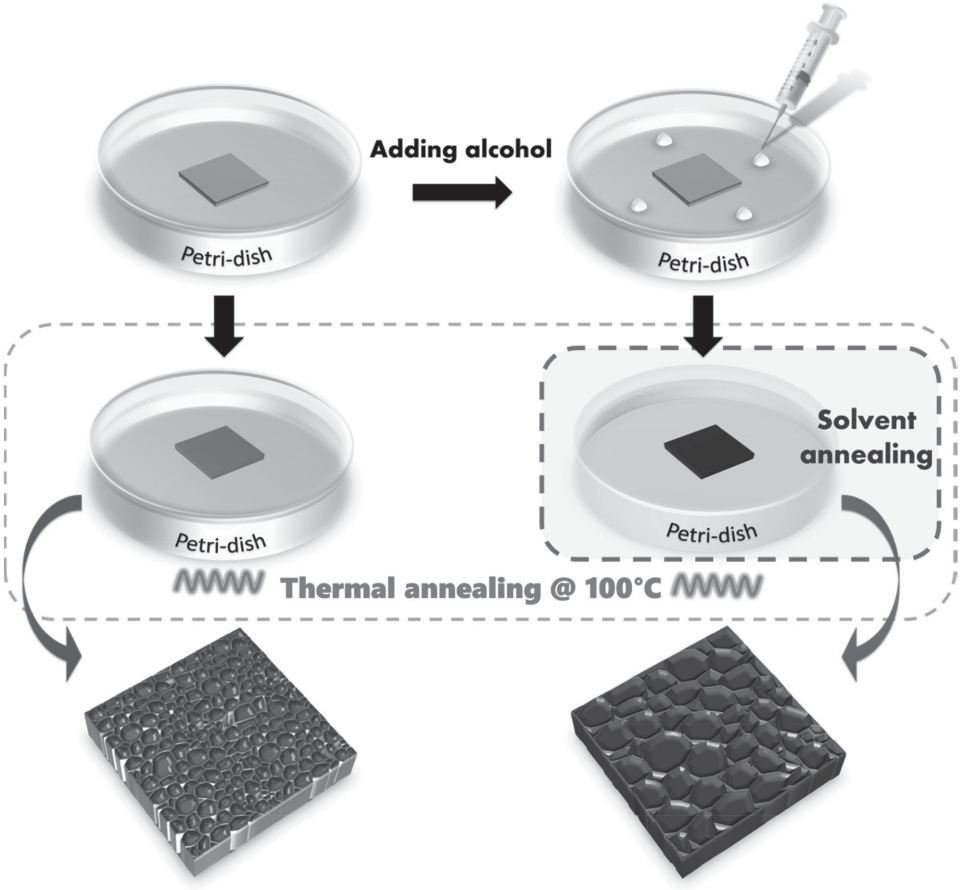

Scheme 1. Schematical illustration of alcohol-vapor solvent annealing and thermal annealing processes.

reported before.[32] Solvent annealing process is carried out in a petri dish filled with alcohol vapor, which is placed on the hotplate at 100 °C to induce the reaction between PbI_2 and CH_3NH_3I. Pristine pero-HSCs where the $CH_3NH_3PbI_3$ thin films are without any solvent annealing treatment are also fabricated for comparison study. Detailed experimental procedures are provided in the Experimental Section.

For the film morphology investigation, 2D GIWAX rather than 1D X-ray diffraction (XRD) is carrier out to probe both lattice structural and crystallographic orientations of the $CH_3NH_3PbI_3$ thin film since 1D XRD can only provide highly ordered structured information. **Figure 1** shows the GIWAX profiles of the $CH_3NH_3PbI_3$ thin films treated by alcohol solvents with different polarities (polarity index, P), methanol (P = 5.1) (the $CH_3NH_3PbI_3$ is represented as the meth-$CH_3NH_3PbI_3$), ethanol (P = 4.3) (the $CH_3NH_3PbI_3$ is represented as the eth-$CH_3NH_3PbI_3$), isopropanol (P = 3.9) (the $CH_3NH_3PbI_3$ is represented as the iso-$CH_3NH_3PbI_3$), and the $CH_3NH_3PbI_3$ thin film without treatment (represented as pristine $CH_3NH_3PbI_3$) for comparison study. The presence of strongly scattered rings in Figure 1a–d indicates that the crystal domains are predominated by polycrystalline (i.e., randomly oriented relative to the substrate), and such crystallographic orientations are not altered by the solvent vapor treatments. Azimuthally integrating the scattering intensities over the scattering vector q (where $q = 4\pi\sin\theta/\lambda$, θ is the half of the scattering angle, λ = 0.116 nm is the X-ray wavelength) affords the GIWAX patterns, as shown in Figure 1e. The distinct peaks at 1.0, 2.0, 2.3, and 2.8 $Å^{-1}$ corresponding to the (110), (220), and (310), (224) lattice planes[4] are in the identical positions for all the $CH_3NH_3PbI_3$ thin films, which indicates that all of the halide perovskite possesses orthorhombic crystal structures.[33] However, the clearly sharper peaks (at 1.0, 2.0, 2.3, and 2.8 $Å^{-1}$) are observed from the $CH_3NH_3PbI_3$ thin films treated by the alcohol vapor, which suggests the perovskite thin films possess increased crystallinity and highly ordered perovskite crystals with fewer low-dimensional defects.[34] Moreover, it is found that the $CH_3NH_3PbI_3$ thin films treated by higher polarity alcohol solvents (methanol and ethanol) show sharper diffraction peaks as compared with those treated with lower polarity alcohol solvent (isopropanol). All these results demonstrate that the $CH_3NH_3PbI_3$ thin films possess large crystallinity and highly ordered orthorhombic crystal structures after treated by the alcohol solvents with high polarity.[35,36]

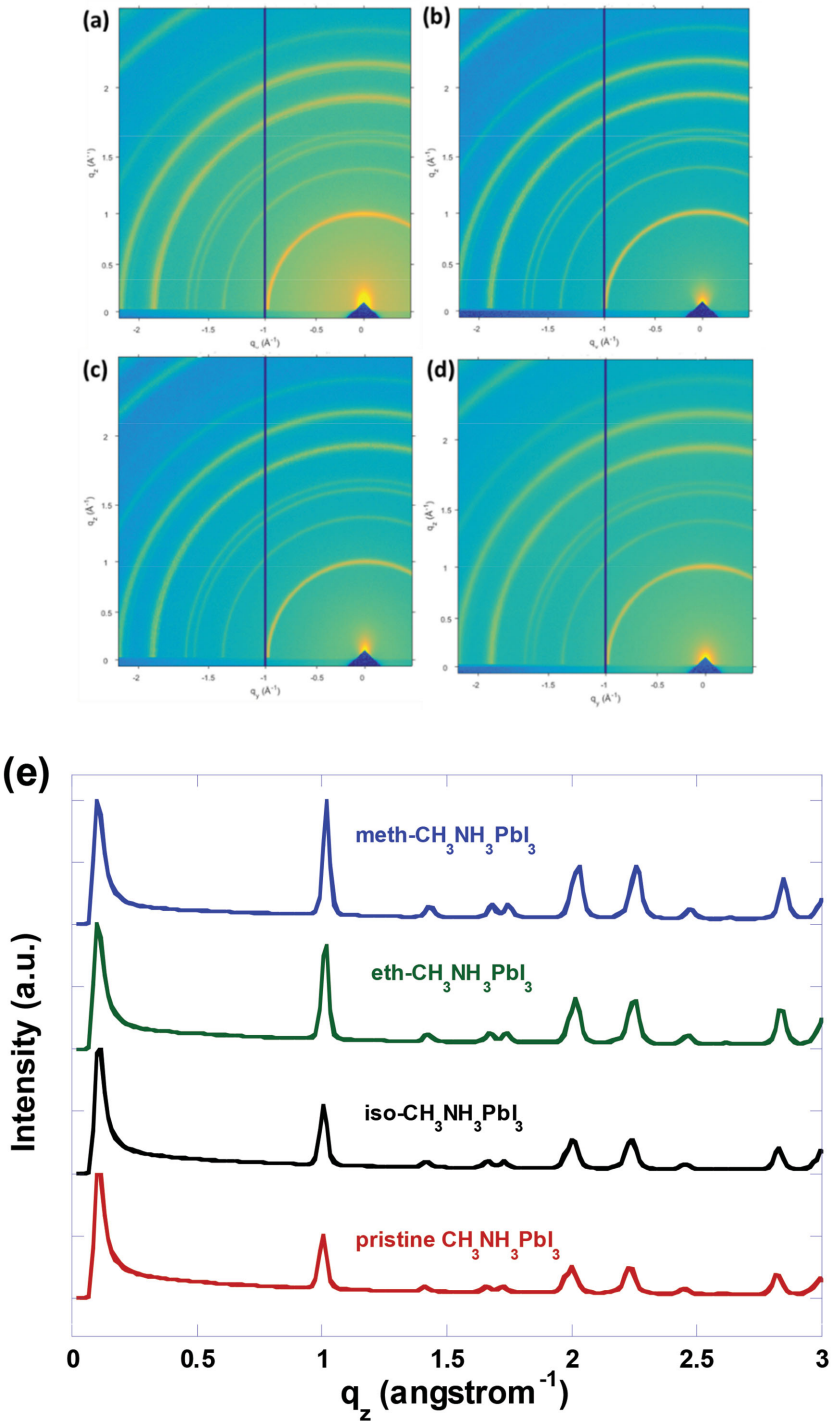

Figure 1. 2D GIWAX profile of a) the pristine $CH_3NH_3PbI_3$ thin film and the $CH_3NH_3PbI_3$ thin films treated with b) methanol, c) ethanol, and d) isopropanol, and e) azimuthally integrated intensity plots of the GIWAXS patterns.

Thin film morphologies of the $CH_3NH_3PbI_3$ layers are further studied by SEM. The results are shown in **Figure 2**a–d. It is found that the pristine $CH_3NH_3PbI_3$ thin film (Figure 2a) exhibits small and randomly distributed perovskite crystals

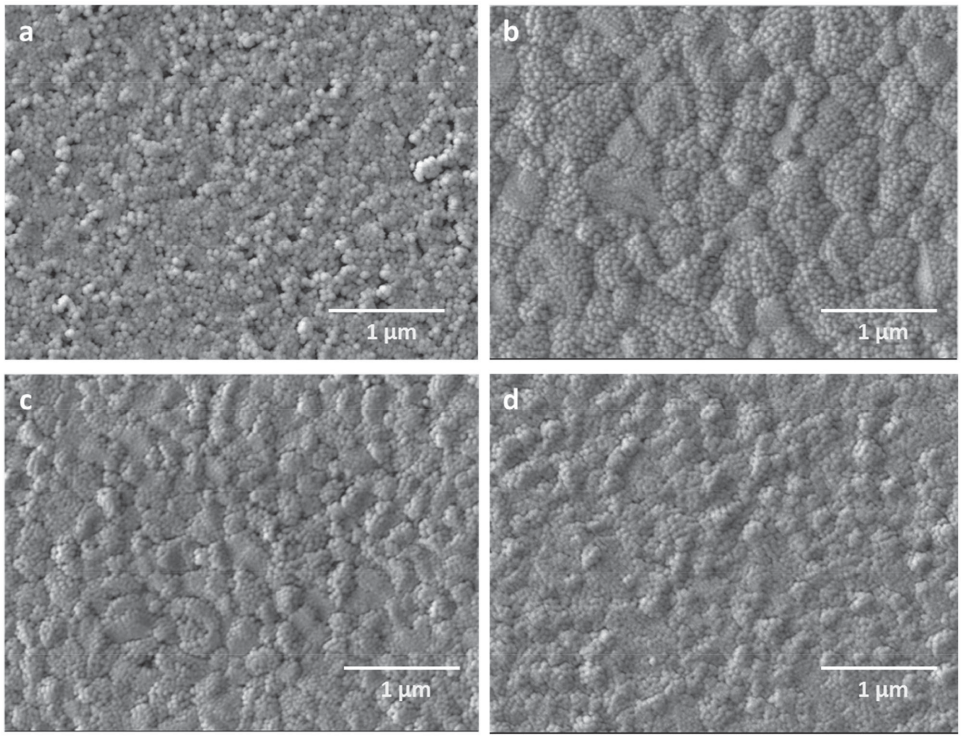

Figure 2. SEM images of a) the pristine $CH_3NH_3PbI_3$ thin film, and the $CH_3NH_3PbI_3$ thin films treated by b) methanol, c) ethanol, and d) isopropanol.

along with large amount of pinholes, which have been demonstrated to be the major issues for poor reproducibility and photocurrent hysteresis behavior in pero-PVs.[37] In clear contrast, much more exquisite $CH_3NH_3PbI_3$ thin films (Figure 2b–d) are formed upon alcohol-vapor annealing treatment, with obviously enhanced grain size, homogeneous distributed crystals, and tremendously minimized defects. The optimized thin film morphology is shown by the meth-$CH_3NH_3PbI_3$ layer, which is consistent with the observations from the GIWAX patterns. The prominently increased grain size (≈500 nm), along with the dramatically reduced pinholes from the meth-$CH_3NH_3PbI_3$ thin film, predicts a suppressed charge carrier recombination that is generally occurred at the grain boundaries and the defect sites.[38,39] It is observed from Figure 2c that the eth-$CH_3NH_3PbI_3$ thin films possess fairly ordered perovskite crystals, but the crystal size (≈300 nm) is smaller than that (≈500 nm) from the meth-$CH_3NH_3PbI_3$ thin films. On the other hand, the iso-$CH_3NH_3PbI_3$ thin films exhibit significantly reduced pinholes while still with inhomogeneous distributed grains.

To inspect the influence of charge transfer process in the $CH_3NH_3PbI_3$ thin films, the time-resolved PL measurements are conducted on the pristine-$CH_3NH_3PbI_3$, the meth-$CH_3NH_3PbI_3$, the eth-$CH_3NH_3PbI_3$ and the iso-$CH_3NH_3PbI_3$ thin films. The PL spectra of above thin films are shown in **Figure 3**. By fitting the data with two exponential decay curves, the lifetime of charge carriers in these four thin films can be obtained.[40] The charge carrier lifetime extracted from the pristine $CH_3NH_3PbI_3$ thin films is 8.7 ns, which is in good agreement with the values reported by others.[41] Under the treatment with alcohol-solvent annealing, the lifetimes are increased to 9.5, 13.7, and 17.1 ns for the iso-$CH_3NH_3PbI_3$ thin films, the eth-$CH_3NH_3PbI_3$ thin films, and the meth-$CH_3NH_3PbI_3$ thin films, respectively. According to the equation of $L_D = \sqrt{D\tau_s}$,[39] where L_D is the charge diffusion length, D is the diffusion constant, and τ_s is the charge carrier lifetime, the longer-lived charge carrier lifetime (τ_s) indicates the increased charge diffusion length (L_D) of the $CH_3NH_3PbI_3$ thin films, which are the consequences of the larger and finer grains of the

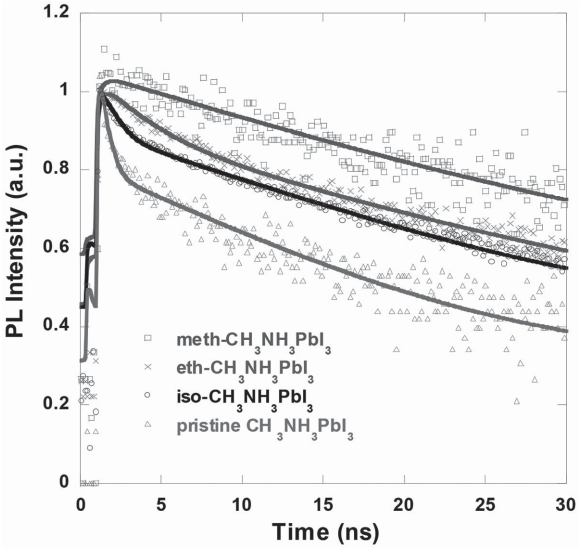

Figure 3. Time-resolved photoluminescence spectra of the pristine $CH_3NH_3PbI_3$ thin film and the $CH_3NH_3PbI_3$ thin films treated with methanol, ethanol, and isopropanol.

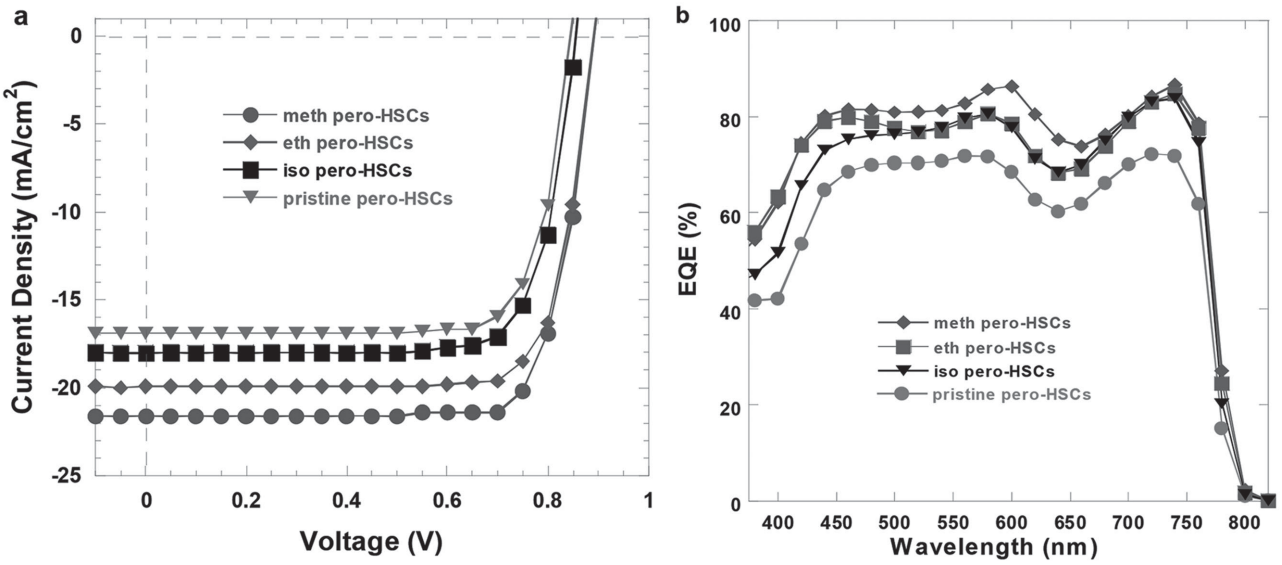

Figure 4. a) *J–V* characteristics of pero-HSCs measured under white light illumination with the light intensity of 100 mW cm^{-2} and b) the EQE spectra of pero-HSCs.

$CH_3NH_3PbI_3$ crystals. Thus increased photocurrent and suppressed dark current, which will ultimately lead to enhanced PCEs in pero-HSCs and detectivity in pero-HPDs, are expected.

A device structure of ITO/PEDOT:PSS/$CH_3NH_3PbI_3$/$PC_{61}BM$/PCBC/Al, where ITO is indium tin oxide as the anode, PEDOT:PSS is poly(3,4-ethylenedioxythiophene):poly(st yrene sulfonate) as the hole extraction layer (HEL), $PC_{61}BM$ is [6,6]-phenyl-C61-butyric acid methyl ester as the electron extraction layer (EEL), PCBC is [6,6]-phenyl-C61-butyric acid (18-crown-6)-2-yl methyl ester (an alcohol-soluble fullerene derivative) as the cathode modification layer,[42] and Al is aluminum as the cathode, is applied for both pero-HSCs and pero-HPDs. In pero-HSCs, where the $CH_3NH_3PbI_3$ thin films without any alcohol vapor treatment are represented as the pristine pero-HSCs, the $CH_3NH_3PbI_3$ thin films treated with methanol, ethanol, and isopropanol are represented as the meth pero-HSCs, the eth pero-HSCs, and the iso pero-HSCs, respectively. The current densities versus voltages (*J–V*) characteristics of pero-HSCs under white light illumination with the light intensity of 100 mW cm^{-2} are shown in **Figure 4**a. **Table 1** summarizes pero-HSCs device performance parameters. The pristine pero-HSCs exhibit a short-circuit current density (J_{SC}) of 16.80 mA cm^{-2}, an open-circuit voltage (V_{OC}) of 0.83 V, a fill factor (FF) of 73.1%, and a corresponding PCE of 10.20%. The PCE observed from the pristine pero-HSCs is in consistent with reported values from the pero-HSCs with a similar device structure.[43] The strikingly raised J_{SC} values are observed from the pero-HSCs where the $CH_3NH_3PbI_3$ thin films are treated by alcohol vapor, reaching the highest value of 21.50 mA cm^{-2} from the meth pero-HSCs. The dramatically increased J_{SC} is attributed to the enhanced grain sizes and highly ordered crystallinities of the $CH_3NH_3PbI_3$ crystals.[44] Furthermore, the FF values are increased from 73.1% for the pristine pero-HSCs to 77.2% for the meth pero-HSCs. Consequently, the PCEs of 11.20 %, 13.30 %, and 14.60 % are observed from the iso pero-HSCs, the eth pero-HSCs, and the meth pero-HSCs, respectively. Noted that over 43% enhancement in PCE is observed from the meth pero-HSCs as compared with that from the pristine pero-HSCs.

Table 1. Device performance parameters of perovskite hybrid solar cells.

	V_{OC} [V]	J_{SC} [mA cm^{-2}]	FF [%]	PCE [%]
pristine pero-HSCs	0.83	16.80	73.1	10.20
iso pero-HSCs	0.85	18.00	73.4	11.20
eth pero-HSCs	0.88	19.90	75.9	13.30
meth pero-HSCs	0.88	21.50	77.2	14.60

V_{OC} is increased from 0.83 V for the pristine pero-HSCs to 0.85, 0.88, and 0.88 V for the iso pero-HSCs, the eth pero-HSCs, and the meth pero-HSCs, respectively. Based on the model of *J–V* characteristics of pero-HSCs with an equivalent circuit consisting of a single diode with a series resistance (R_S) and shunt resistance (R_{SH}), along with a parallel photocurrent source (J_{ph}), the equation $J = J_0\left[\exp\left(\frac{q(V-R_SAJ)}{nkT}\right)-1\right]+\frac{V-R_SAJ}{R_{SH}A}-J_{ph}(V)$ can be obtained, where q is the electron charge, k is the Boltzmann's constant, T is the temperature, n is the ideality factor (close to 2 for pero-HSC),[45] J_0 is the reverse dark current density, J_{ph} is the voltage-dependent photocurrent produced by the cells, V is the applied voltage, and A is the device area. Under open circuit condition, where $J = 0$ and $J_{ph} = J_{SC}$, the above equation can be rearranged to $V_{OC} \approx \frac{nkT}{q}\ln\left(\frac{J_{SC}}{J_0}\right)$. Thus, it is concluded that the decreased dark currents in the reverse bias region (see Figure 8a) should be the origin of the enhanced V_{OC} for pero-HSCs.

The external quantum efficiency (EQE) spectra, which specify the ratio of the extracted electrons to the incident phowtons at a given wavelength, of pero-HSCs are measured and the results are presented in Figure 4b. The pristine pero-HSCs show a wide photoresponse from 375 to 800 nm, with EQE values over 70% ranging from 450 to 600 nm, and from

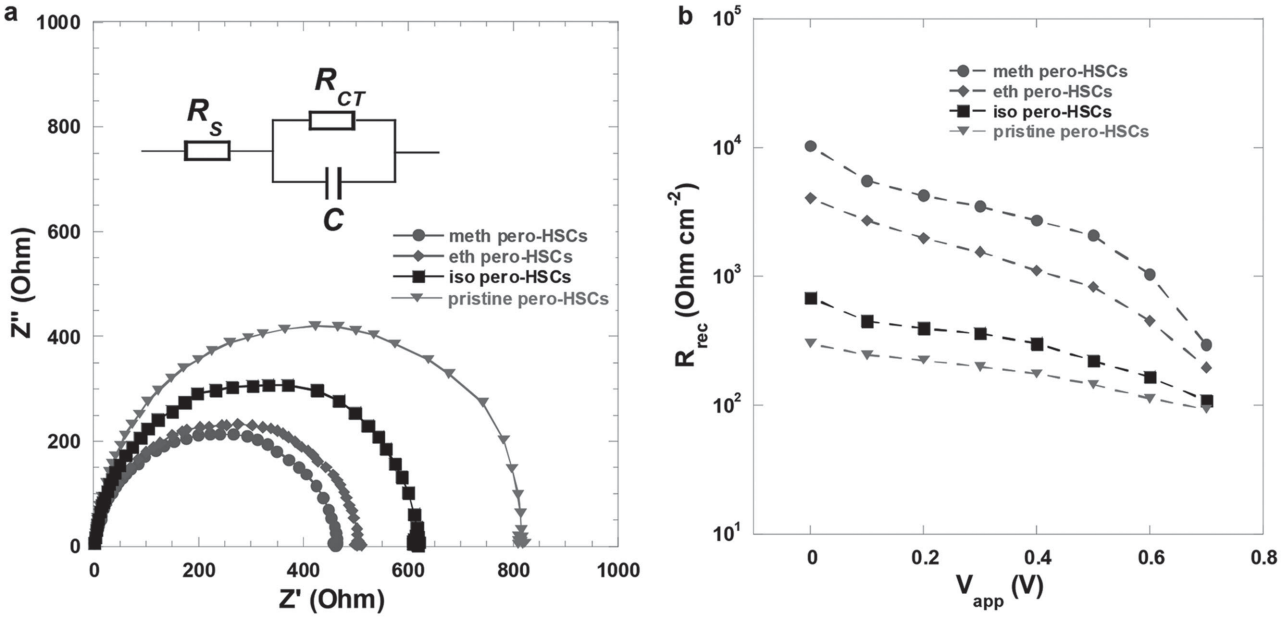

Figure 5. a) Nyquist plots of pero-HSCs measured in dark and at an applied voltage close to the open-circuit voltage of pero-HSCs. b) Recombination resistances of pero-HSCs measured under white illumination with the light intensity of 100 mW cm^{-2}.

700 to 750 nm, which reflects the weakly bounded excitons in the $CH_3NH_3PbI_3$ thin films and effective charge transfer process in pero-HSCs.[14] The EQE values from the pero-HSCs where the $CH_3NH_3PbI_3$ thin films are treated with alcohol-vapor annealing are increased to over 80%, reaching the highest value of 87% from the meth pero-HSCs. It is also noteworthy that the EQE spectra from 550 to 600 nm for the pero-HSCs where the $CH_3NH_3PbI_3$ thin films are treated by alcohol-vapor are redshifted as compared with that of the pristine pero-HSCs, further indicating the formation of highly ordered $CH_3NH_3PbI_3$ crystals induced by alcohol-vapor annealing.[43] Integration of the EQE spectra over the wavelength range from 375 to 800 nm affords the photocurrent of 14.80, 17.50, 18.70, and 20.60 mA cm^{-2} for the pristine pero-HSCs, the iso pero-HSC, the eth pero-HSCs, and the meth pero-HSCs, respectively. These estimated J_{SC} values are in good agreement with the J_{SC} values from J–V characteristics (Figure 4a).

Impedance spectroscopy (IS) is carried out to investigate charge transfer properties in pero-HSCs. The IS is conducted in dark at an applied voltage close to V_{OC}. Under these conditions, the recombination resistance (R_{rec}) from the HEL to the EEL reaches the lowest value ($R_{rec} \ll R_{CT}$, R_{CT} is the charge transfer resistance from HTL to ETL). Therefore the equivalent circuit can be simplified to the circuit model shown in the inset of **Figure 5**a, where R_S is the sheet resistance of the conductive electrode.[46] In our study, all pero-HSCs possess the same device structure, the R_S is assumed to be the same. Thus, the major difference is R_{CT} induced by various crystal morphologies of the $CH_3NH_3PbI_3$ active layer. From the Nyquist plots of pero-HSCs shown in Figure 5a, R_{CT} of 810, 610, 500, and 460 Ω are obtained for the pristine pero-HSCs, the iso pero-HSCs, the eth pero-HSCs, and the meth pero-HSCs, respectively. A large R_{CT} for the pristine pero-HSCs is resulted from the inferior $CH_3NH_3PbI_3$ crystal morphology, including small-sized and randomly distributed $CH_3NH_3PbI_3$ grains and large amount of defect-assisted traps. With the improved quality of the $CH_3NH_3PbI_3$ crystals upon the solvent annealing treatment, charge carrier transfer process is greatly facilitated, which leads to the dramatically decreased R_{CT}. As a result, high J_{SC} are observed from the pero-HSCs where the $CH_3NH_3PbI_3$ thin films are treated by alcohol vapor.

The charge recombination resistances, which are inversely proportional to the charge carrier recombination rate, as a function of the applied voltages are also extracted from the Nyquist plot in the low-frequency region.[47] The results are shown in Figure 5b. It is found that the charge carrier recombination resistances of the iso pero-HSCs, the eth pero-HSCs, and the meth pero-HSCs are larger than those of the pristine pero-HSCs, which is in accordance with the GIWAX, SEM, and time-resolved PL results. These results further demonstrate that the $CH_3NH_3PbI_3$ thin films have a tendency to form highly ordered crystals with large grain size after treated by the alcohol solvents with high polarity, resulting in enhanced charge carrier diffusion length and suppressed charge recombination process. Moreover, it is found that even at large-bias region, the charge carrier recombination resistances of the pero-HSCs where the $CH_3NH_3PbI_3$ thin films are treated by alcohol vapor are higher than those of the pristine pero-HSCs, which is consistent with the enlarged V_{OC} from the pero-HSCs where the $CH_3NH_3PbI_3$ thin films are treated by alcohol-vapor annealing (as shown in Figure 4a).[48]

The reproducibility is one of the significant issues needed to be addressed in pero-HSCs.[49] In order to study the reproducibility of pero-HSCs, over 200 pero-HSCs are fabricated and characterized. **Figure 6** presents the histograms of the PV parameters of the pristine pero-HSCs and the meth pero-HSCs. As indicated in Figure 6, the reproducibilities of V_{OC}, J_{SC}, FF, and PCE are fairly high, with small relative standard deviation of 0.7 %, which is dramatically lower than that of the pristine-

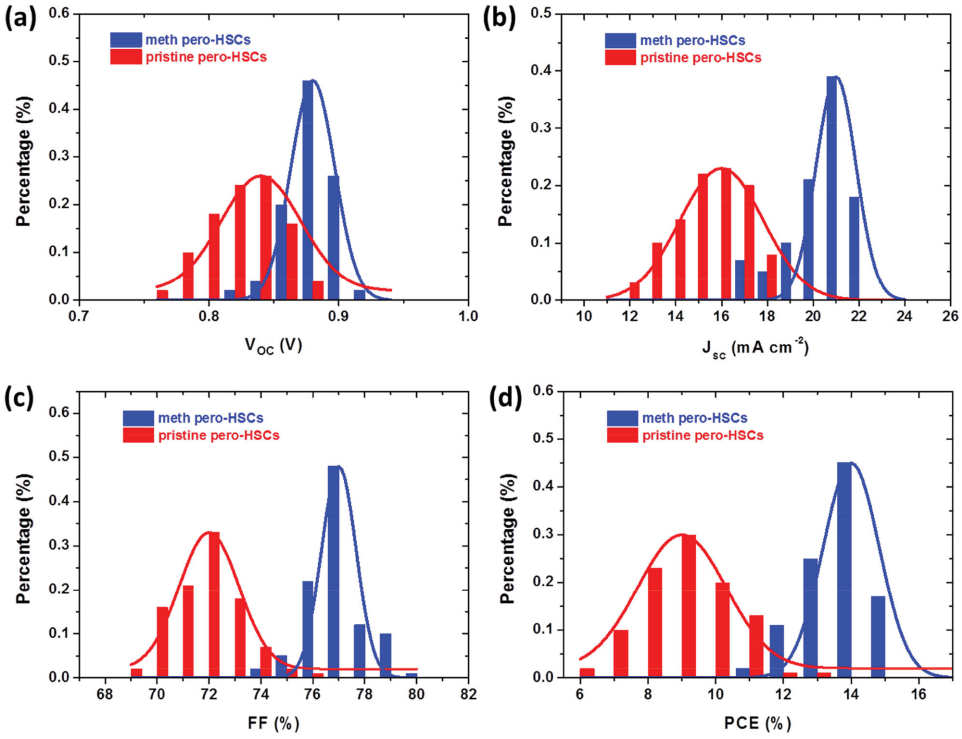

Figure 6. Histograms of the photovoltaic parameters of pero-HSCs a) V_{OC}, b) J_{SC}, c) FF, and d) PCE (the number of pero-HSCs is 200).

HSCs (1.7%). Therefore, it is concluded that a fine-formed and highly ordered $CH_3NH_3PbI_3$ crystal is of paramount importance to the high reproducibility of pero-HSCs.

The photocurrent hysteresis behavior, majorly originated from the defect-assisted traps in perovskite grains,[50–52] is another critical issue of pero-HSCs. To investigate the effects of solvent annealing treatment on the photocurrent hysteresis behaviors of pero-HSCs, different scan rates (a high scan rate of 0.5 V s^{-1} and a low scan rate of 20 mV s^{-1}) and scan directions (reverse scan: from a positive bias to a negative bias, and forward scan: from a negative bias to a positive bias) are performed on pero-HSCs. **Figure 7** presents the *J–V* characteristics of pristine pero-HSCs and the meth pero-HSCs under different scan rates and different scan directions. As compared with those of the pristine pero-HSCs, highly consistent *J–V* characteristics regardless of the scan rates and scan directions are observed from the meth pero-HSCs, which manifests that the photocurrent hysteresis of pero-HSCs is minimized due to the greatly reduced defects in the $CH_3NH_3PbI_3$ thin films by methanol vapor treatment.

The pero-HPDs with a device structure of ITO/PEDOT:PSS/$CH_3NH_3PbI_3$/$PC_{61}BM$/PCBC/Al are also investigated. The *J–V* characteristics of pero-HPDs measured at room temperature under the illumination of monochromatic light at a wavelength (λ) of 500 nm with the light intensity of 0.48 mW cm^{-2} and in dark are shown in **Figure 8**a. It is obvious that the photocurrent densities (J_{ph}) of the meth pero-HPDs, the eth pero-HPDs, and the iso pero-HPDs are greatly increased over those of the pristine pero-HPDs, which indicate charge transfer processes are facilitated in the $CH_3NH_3PbI_3$ thin films by alcohol-vapor treatment. Also, the dark current densities (J_d) of the pero-HPDs where the $CH_3NH_3PbI_3$ thin films are treated by alcohol vapor are lower than those of the pristine pero-HPDs from the reverse to the forward bias region. The decreased J_d in the reverse region indicates the leakage currents from the pero-HPDs are suppressed, which is originated from the reduced defects in the $CH_3NH_3PbI_3$ thin film. The decreased J_d in the forward bias region (0–0.7 V) implies the charge carrier recombination in the pero-HPDs is restrained,[53] which is in good agreement with observed PL results and the R_{rec} versus V characteristics.

The responsivity (R) and the detectivity (D^*) of pero-HPDs at λ = 500 nm and under an external bias at −0.5 V can be

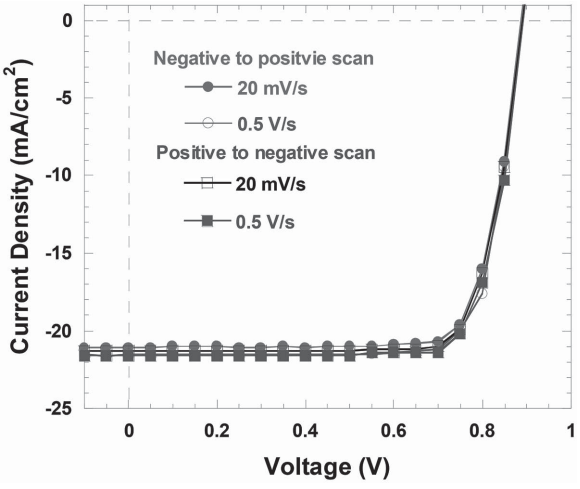

Figure 7. *J–V* characteristics of pero-HSCs under different scan rates and scan directions.

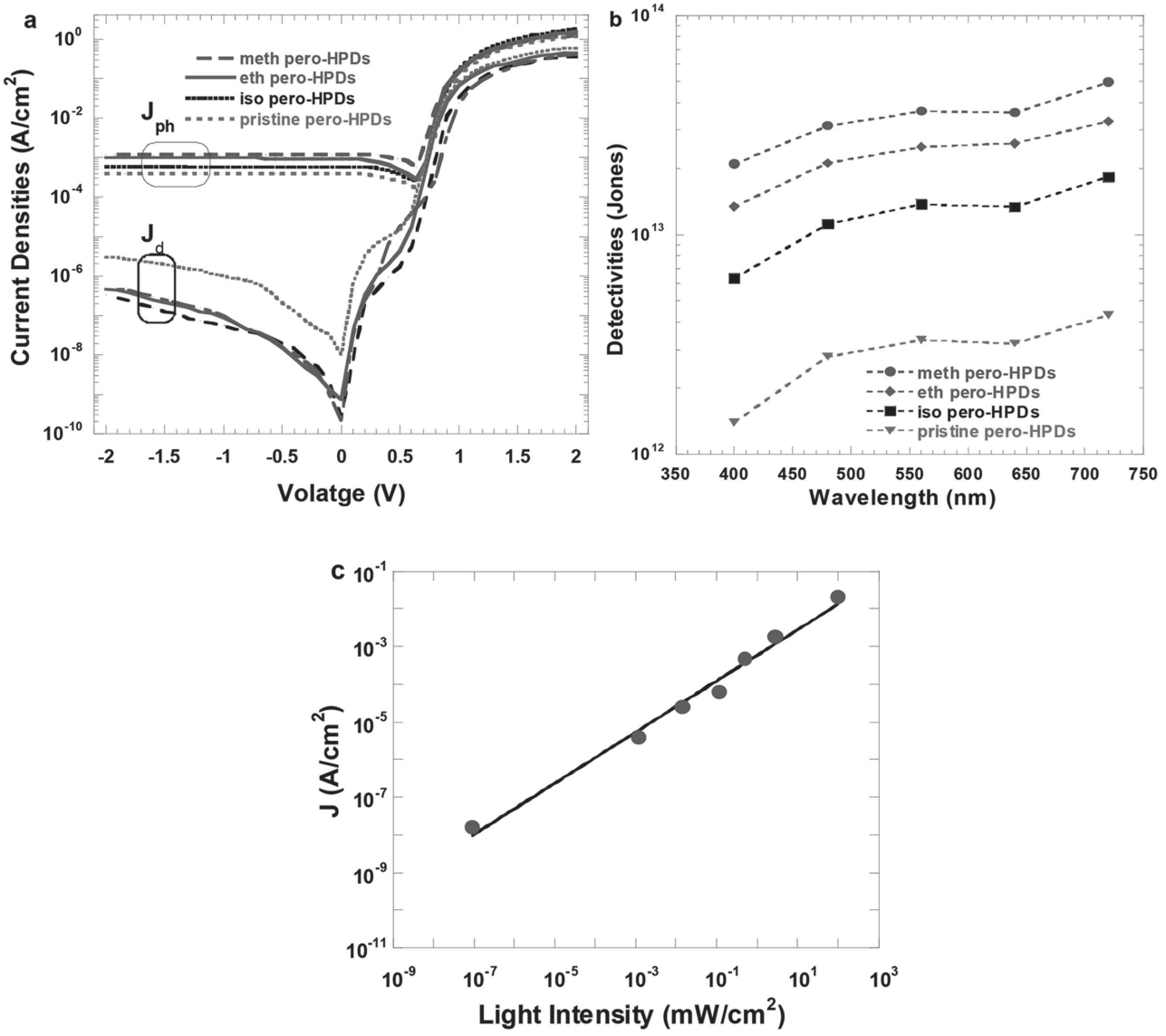

Figure 8. a) *J–V* characteristics of pero-HPDs measured in dark and under monochromatic light at the wavelength of 500 nm with the light intensity of 0.48 mW cm^{-2}. b) *D** (@–0.5 V) versus the wavelength for pero-HPDs. c) Linear dynamic range of pero-HSCs.

estimated according to the equation $R = \frac{J_{ph}}{L_{light}}$,[50] where L_{light} is the light intensity, and the equation $D^* = R/\sqrt{2qJ_d}$,[54] where q is the absolute value of electron charge. Both R and D^* are the device performance parameters used to evaluate PDs,[54] which are summarized in **Table 2**. It is noticed that both R and D^* are largely increased upon the alcohol vapor treatment, among which, the highest R of 2.71 A W^{-1} and D^* of 3.4 × 10^{13} Jones are obtained from the meth pero-HPDs. D^* under different wavelength were also measured, as plotted in Figure 8b. An overall enhanced D^* in the visible region is observed from the solvent-treated pero-HPDs, which is a consequence of both improved photocurrent and reduced dark current.

Based on the photocurrent densities versus the incident light intensities as shown in Figure 8c, the linear dynamic range (LDR) or photosensitivity linearity (typically quoted in dB), which is another device performance parameter used to evaluate PDs, of the meth pero-HPDs, is estimated according to the equation of $\mathrm{LDR} = 20\log(J^*_{ph}/J_d)$,[55] where $K^*_{\pi 0}$ is the photocurrent measured at the light intensity of 1 mW cm^{-2}. At room temperature, the LDR is ≈105 dB for the meth pero-PDs. This large LDR is

Table 2. Device performance parameters of perovskite hybrid photodetectors. J_{ph} and J_d are measured at λ = 500 nm with a light intensity of 0.48 mW cm^{-2} and at a bias of –0.5 V.

	J_{ph} [A cm^{-2}]	J_d [A cm^{-2}]	R [A W^{-1}]	D^* [Jones]
pristine pero-HPDs	3.8×10^{-4}	2.1×10^{-7}	0.79	3.0×10^{12}
iso pero-HPDs	5.7×10^{-4}	2.3×10^{-8}	1.18	1.3×10^{12}
eth pero-HPDs	8.5×10^{-4}	1.8×10^{-8}	1.77	3.1×10^{13}
meth pero-HPDs	1.3×10^{-3}	1.6×10^{-8}	2.71	3.4×10^{13}

comparable to that of Si PDs (120 dB, at 77 K) and is significantly higher than InGaAs PDs (66 dB, at 4.2 K).[56] Thus, at room temperature, the device performance parameters of the meth pero-HPDs are comparable to those of Si PDs and InGaAs PDs as well.

3. Conclusion

In summary, we performed alcohol vapors annealing treatment on the $CH_3NH_3PbI_3$ thin films, aiming to improve the crystal growth and increase the grain size of the $CH_3NH_3PbI_3$ crystal, thus boosting the device performance of perovskite hybrid PVs. By selectively controlling the CH_3NH_3I precursor, fine-tuning the $CH_3NH_3PbI_3$ crystal growth can be realized, which generates large-grain size, higher crystallinity, and pinhole-free $CH_3NH_3PbI_3$ thin films. As a result, high performance perovskite hybrid PVs including pero-HSCs and photodetectors are observed. It is also found that the $CH_3NH_3PbI_3$ thin films possess more highly ordered crystal formation upon treated by alcohol solvents with higher polarity (methanol and ethanol) than their lower polarity analog (2-propanol). The highly ordered $CH_3NH_3PbI_3$ crystals would be favorable for the charge transfer process in the perovskite PVs. As a result, greatly increased efficiencies with excellent reproducibility and eliminated hysteresis behavior are observed from pero-HSCs, and significantly improved detectivities are realized in pero-HPDs. Thus, our method provides a facile way to boost the device performance of perovskite PVs.

4. Experimental Section

Materials: $PC_{61}BM$ (99.5%) was purchased from Solenne BV and used as received without further treatment. Lead iodide (PbI_2, 99.999%), anhydrous DMF, methanol (CH_3OH, anhydrous, >99.5%), ethanol (CH_3CH_2OH, anhydrous, >99.5%), 2-propanol ($CH_3CHOHCH_3$, anhydrous, >99.5%), and anhydrous chlorobenzene (99.8%) were purchased from Sigma-Aldrich and used as received. Methylammonium iodide (MAI, CH_3NH_3I) was synthesized by hydroiodic acid and methylamine in our laboratory. PCBC was provided by Prof. M. Lei and Y. F. Li.[41]

Perovskite Precursor: PbI_2 was dissolved into DMF solvent with a concentration of 400 mg mL^{-1}. Then, PbI_2 DMF solution was magnetically stirred at 70 °C for about 12 h till the cloudy solution yields to transparent yellow solution. CH_3NH_3I (MAI) was dissolved in ethanol with a concentration of 35 mg mL^{-1}.

Pero-HSCs and pero-HPDs Fabrication: The PEDOT:PSS layer was spin-coated onto precleaned and UV-treated ITO substrates, followed with thermal-annealing at 150 °C for 10 min in the air and then transferred into the glovebox with nitrogen atmosphere. PbI_2 layer was spin-cast on the top of the preheated (70 °C) ITO/PEDOT:PSS substrates from the warm (70 °C) PbI_2 solution at a spin-speed of 3000 rpm for 25 s with an acceleration time of 2 s. Then the substrates are placed on the hotplate at 70 °C for 10 min and then cooled down to room temperature. MAI layer is then spin-coated on the top of the PbI_2 layer from the MAI ethanol solution at a spin-speed of 3000 rpm for 25 s with an acceleration time of 2 s, followed by transferring the thin films onto the hotplate at 100 °C for pristine perovskite PVs (pero-HSCs and pero-HPDs). The thermal annealing process lasts for 2 h.

For Alcohol-Vapor Annealing Treatment: First, the as-casted $CH_3NH_3PbI_3$ thin films were placed into the petri-dish with a volume of 100 mL. Second, methanol, ethanol, and isopropanol solvents were dripped into three identical petri-dishes, respectively, and the vapor concentration of 20% was made sure in the petri-dish after evaporation of the solvents (i.e., for ensuring 20% ethanol vapor concentration, the volume of ethanol added into the petri-dish should be $V = 100\,mL \times 20\% \times \frac{\rho_V}{\rho_l} = 40\,\mu L$, where $\rho_V = 1.59\,kg\,m^{-3}$ is the density of the ethanol vapor and $\rho_l = 0.789\,g\,cm^{-3}$ is the density of the ethanol solvent); lastly, the petri-dishes were put on the hotplate and thermal annealed at 100 °C for 2 h to convert PbI_2 and MAI into $CH_3NH_3PbI_3$. The optimized vapor concentration (20%) for three alcohols were found by investigating the effects of a series vapor concentrations on the pero-HSCs efficiencies; the results are shown in Figure S1 and Table S1 (Supporting Information).

After the $CH_3NH_3PbI_3$ thin films were treated by alcohol vapors, the $PC_{61}BM$ EEL was spin-cast on the top of the $CH_3NH_3PbI_3$ layer from 20 mg mL^{-1} chlorobenzene solution. After then, the PCBC layer was cast on the top of the $PC_{61}BM$ EEL from 0.2 mg mL^{-1} ethanol solution. Lastly, a 100 nm thick aluminum was thermally deposited through a shadow mask in the vacuum with the press of 4×10^{-6} mbar. The device area was measured to be 0.16 cm^2.

Thin Film Characterization: GIWAX diffraction spectra were carried out in beamline 8-ID-E, Advanced Photon Source, Argonne National Lab. SEM images were measured by Model JEOL-7401 Japan electron optics laboratory (JEOL). In the time-resolved PL measurement, the samples were excited by a pulsed laser (SuperK NKT Photonics, Birkerod, Denmark) with a wavelength of 640 nm (power 25 nW), and the PL photons went through a band pass filter (697 ± 70 nm) and were counted by time-correlated single photon counting module (Picoharp 300, PicoQuant, Berlin, Germany).

Pero-PVs Characterization: The *J–V* characteristics of pero-PVs were carried out on a Keithley model 2400 source measure unit with a light intensity of 100 mW cm^{-2} (for pero-HSCs) and under a monochromatic light at 500 nm with a light intensity of 0.48 mW cm^{-2} (for pero-HPDs). The EQE was obtained by using the solar cell quantum efficiency measurement system (QEX10) from PV measurements with a 300 W steady-state xenon lamp as the source light. The impedance spectra (IS) of pero-HSCs were obtained using an HP 4194A impedance/gain-phase analyzer under dark condition, with an oscillating voltage of 10 mV from 5 Hz to 10^5 Hz. Pero-HSCs were held at the voltage closing to the corresponding V_{OC}, while the IS were carried out.

Supporting Information

Supporting Information is available from the Wiley Online Library or from the author.

Acknowledgements

The authors would like to thank NSF (EECS 540089) and Air Force Defense Research Sciences Program (FA9550-15-1-0292) for financial support. The authors thank Prof. Yongfan Li in the Chemistry Institute at the Chinese Academic Science and Prof. Ming Lei in the Department of Chemistry at the Zhejiang University for providing PCBC material. The authors would also like to thank Dr. Zhang Jiang for assistance with the GIWAXS measurements through the U.S. Department of Energy, Office of Science, Office of Basic Energy Sciences, under Contract DE-AC02-06CH11357.

Received: September 22, 2015
Published online: November 20, 2015

[1] A. Mei, X. Li, L. Liu, Z. Ku, T. Liu, Y. Rong, M. Xu, M. Hu, J. Chen, Y. Yang, M. Grätzel, H. Han, *Science* **2014**, *345*, 295.

[2] L. Etgar, P. Gao, Z. Xue, Q. Peng, A. K. Chandiran, B. Liu, M. K. Nazeeruddin, M. Grätzel, *J. Am. Chem. Soc.* **2012**, *134*, 17396.
[3] H.-S. Kim, C.-R. Lee, J.-H. Im, K.-B. Lee, T. Moehl, A. Marchioro, S.-J. Moon, R. Humphry-Baker, J.-H. Yum, J. E. Moser, M. Grätzel, N.-G. Park, *Sci. Rep.* **2012**, *2*, 1.
[4] J. Qiu, Y. Qiu, K. Yan, M. Zhong, C. Mu, H. Yan, S. Yan, *Nanoscale* **2013**, *5*, 3245.
[5] M. M. Lee, J. Teuscher, T. Miyasaka, T. N. Murakami, H. J. Snaith, *Science* **2012**, *338*, 643.
[6] H.-S. Kim, J.-W. Lee, N. Yantara, P. P. Boix, S. A. Kulkarni, S. Mhaisalkar, M. Grätzel, N.-G. Park, *Nano Lett.* **2013**, *13*, 2412.
[7] L. Dou, Y. M. Yang, J. You, Z. Hong, W. H. Chang, G. Li, Y. Yang, *Nat. Commun.* **2014**, *5*, 5404.
[8] C. Liu, K. Wang, C. Yi, X. Shi, P. Du, A. W. Smith, A. Karim, X. Gong, *J. Mater. Chem. C* **2015**, *3*, 6600.
[9] C. Liu, K. Wang, P. Du, E. Wang, X. Gong, A. J. Heeger, *Nanoscale* **2015**, *7*, 16460.
[10] R. Dong, Y. Fang, J. Chae, J. Dai, Z. Xiao, Q. Dong, Y. Yuan, A. Centrone, X. C. Zeng, J. Huang, *Adv. Mater.* **2015**, *27*, 1912.
[11] Q. Lin, A. Armin, D. M. Lyons, P. L. Burn, P. Meredith, *Adv. Mater.* **2015**, *27*, 2060.
[12] J. H. Im, C. R. Lee, J. W. Lee, S. W. Park, N. G. Park, *Nanoscale* **2011**, *3*, 4088.
[13] M. M. Lee, J. Teuscher, T. Miyasaka, T. N. Murakami, H. J. Snaith, *Science* **2012**, *338*, 643.
[14] K. G. Stamplecoskie, J. S. Manser, P. V. Kamat, *Energy Environ. Sci.* **2015**, *8*, 208.
[15] J. H. Heo, D. H. Song, H. J. Han, S. Y. Kim, J. H. Kim, D. Kim, H. W. Shin, T. K. Ahn, C. Wolf, T.-W. Lee, S. H. Im, *Adv. Mater.* **2015**, *27*, 3424.
[16] J. H. Park, J. Seo, S. Park, S. S. Shin, Y. C. Kim, N. J. Jeon, H.-W. Shin, T. K. Ahn, J. H Noh, S. C. Yoon, C. S. Hwang, S. I. Seok, *Adv. Mater.* **2015**, *27*, 4013.
[17] Y. Shao, Z. Xiao, C. Bi, Y. Yuan, J. Huang, *Nat. Commun.* **2014**, *5*, 5784.
[18] J. A. Christians, J. S. Manser, P. V. Kamat, *J. Phys. Chem. Lett.* **2015**, *6*, 2086.
[19] H. L. Hsu, C. P. Chen, J. Y. Chang, Y. Y. Yu, Y. K. Shen, *Nanoscale* **2014**, *6*, 10281.
[20] Q. Chen, H. Zhou, Z. Hong, S. Luo, H. S. Duan, H. H. Wang, Y. Liu, G. Li, Y. Yang, *J. Am. Chem. Soc.* **2013**, *136*, 622.
[21] P. W. Liang, C. Y. Liao, C. C. Chueh, F. Zuo, S. T. Williams, X. K. Xin, J. Lin, A. K. Y. Jen, *Adv. Mater.* **2014**, *26*, 3748.
[22] C. Zuo, L. Ding, *Nanoscale* **2014**, *6*, 9935.
[23] N. J. Jeon, J. H. Noh, Y. C. Kim, W. S. Yang, S. Ryu, S. Il. Seok, *Nat. Mater.* **2014**, *13*, 897.
[24] H. B. Kim, H. Choi, J. Jeong, S. Kim, B. Walker, S. Song, J. Y. Kim, *Nanoscale* **2014**, *6*, 6679.
[25] Z. Xiao, Q. Dong, C. Bi, Y. Shao, Y. Yuan, J. Huang, *Adv. Mater.* **2014**, *26*, 6503.
[26] Y. Wu, A. Islam, X. Yang, C. Qin, J. Liu, K. Zhang, W. Peng, L. Han, *Energy Environ. Sci.* **2014**, *7*, 2934.
[27] E. Zheng, X. F. Wang, J. Song, L. Yan, W. Tian, T. Miyasaka, *ACS Appl. Mater. Interfaces* **2015**, *7*, 18156.
[28] J. H. Heo, H. J. Han, D. Kim, T. K. Ahn, S. H. Im, *Energy Environ. Sci.* **2015**, *8*, 1602.
[29] J. Jo, S. S. Kim, S. I. Na, B. K. Yu, D. Y. Kim, *Adv. Funct. Mater.* **2009**, *19*, 866.
[30] C. Wehrenfennig, G. E. Eperon, M. B. Johnston, H. J. Snaith, L. M. Herz, *Adv. Mater.* **2014**, *26*, 1584.
[31] Y. Yamada, T. Nakamura, M. Endo, A. Wakamiya, Y. Kanemitsu, *J. Am. Chem. Soc.* **2014**, *136*, 11610.
[32] Z. Xiao, C. Bi, Y. Shao, Q. Dong, Q. Wang, Y. Yuan, C. Wang, Y. Gao, J. Huang, *Energy Environ. Sci.* **2014**, *7*, 2619.
[33] W. J. Yin, T. Shi, Y. Yan, *Adv. Mater.* **2014**, *26*, 4653.
[34] Q. Chen, H. Zhou, T. B. Song, S. Luo, Z. Hong, H. S. Duan, L. Dou, Y. Liu, Y. Yang, *Nano Lett.* **2014**, *14*, 4158.
[35] Y. Wang, T. Gould, J. F. Dobson, H. Zhang, H. Yang, X. Yao, H. Zhao, *Phys. Chem. Chem. Phys.* **2014**, *16*, 1424.
[36] T. Baikie, Y. Fang, J. M. Kadro, M. Schreyer, F. Wei, S. G. Mhaisalkar, M. Graetze, T. J. White, *J. Mater. Chem. A* **2013**, *1*, 5628.
[37] Y. J. Jeon, S. Lee, R. Kang, J. E. Kim, J. S. Yeo, S. H. Lee, S. S. Kim, J. M. Yun, D. Y. Kim, *Sci. Rep.* **2014**, *4*, 6953.
[38] E. Edri, S. Kirmayer, A. Henning, S. Mukhopadhyay, K. Gartsman, Y. Rosenwaks, G. Hodes, D. Cahen, *Nano Lett.* **2014**, *14*, 1000.
[39] H. S. Kim, N. G. Park, *J. Phys. Chem. Lett.* **2014**, *5*, 2927.
[40] D. C. Reynolds, D. C. Look, B. Jogai, J. E. Hoelscher, R. E. Sherriff, M. T. Harris, M. J. Callahan, *J. Appl. Phys.* **2000**, *88*, 2152.
[41] S. D. Stranks, G. E. Eperon, G. Grancini, C. Menelaou, M. J. Alcocer, T. Leijtens, L. M. Herz, A. Petrozza, H. J. Snaith, *Science* **2013**, *342*, 341.
[42] X. Liu, W. Jiao, M. Lei, Y. Zhou, B. Song, Y. Li, *J. Mater. Chem. A* **2015**, *3*, 9278.
[43] K. Wang, C. Liu, P. Du, H. L. Zhang, X. Gong, *Small* **2015**, *11*, 3369.
[44] W. Nie, H. Tsai, R. Asadpour, J. C. Blancon, A. J. Neukirch, G. Gupta, J. J. Crochet, M. Chhowalla, S. Tretiak, M. A. Alam, H. L. Wang, A. D. Mohite, *Science* **2015**, *347*, 522.
[45] S. Agarwal, M. Seetharaman, N. K. Kumawat, A. S. Subbiah, S. K. Sarkar, D. Kabra, M. A. C. Namboothiry, P. R. Nair, *J. Phys. Chem. Lett.* **2014**, *5*, 4115.
[46] N. Li, B. E. Lassiter, R. R. Lunt, G. Wei, S. R. Forrest, *Appl. Phys. Lett.* **2009**, *94*, 023307.
[47] J.-S. Kim, W.-S. Chung, K. Kim, D. Y. Kim, K.-J. Paeng, S. M. Jo, S.-Y. Jang, *Adv. Funct. Mater.* **2010**, *20*, 3538.
[48] C. Liu, X. Hu, C. Zhong, M. Huang, K. Wang, Z. Zhang, X. Gong, C. Yong, A. J. Heeger, *Nanoscale* **2014**, *6*, 14297.
[49] F. F. Santiago, G. G. Belmonte, I. M. Seróa, J. Bisquert, *Phys. Chem. Chem. Phys.* **2011**, *13*, 9083.
[50] Y. Wu, A. Islam, X. Yang, C. Qin, J. Liu, K. Zhang, W. Peng, L. Han, *Energy Environ. Sci.* **2014**, *7*, 2934.
[51] E. L. Unger, E. T. Hoke, C. D. Bailie, W. H. Nguyen, A. R. Bowring, T. Heumuller, M. G. Christoforod, M. D. McGehee, *Energy Environ. Sci.* **2014**, *7*, 3690.
[52] W. Tress, N. Marinova, T. Moehl, S. M. Zakeeruddin, M. K. Nazeeruddin, M. Grätzel, *Energy Environ. Sci.* **2015**, *8*, 995.
[53] H. J. Snaith, A. Abate, J. M. Ball, G. E. Eperon, T. Leijtens, N. K. Noel, S. D. Stranks, J. T.-W. Wang, K. Wojciechowski, W. Zhang, *J. Phys. Chem. Lett.* **2014**, *5*, 1511.
[54] Q. Wang, Y. Shao, Q. Dong, Z. Xiao, Y. Yuan, J. Huang, *Energy Environ. Sci.* **2014**, *7*, 2359.
[55] X. Gong, M. Tong, Y. Xia, W. Cai, S. Ji, Y. Cao, G. Yu, C. L. Shieh, B. Nilsson, A. J. Heeger, *Science* **2009**, *325*, 1665.
[56] I. Howard, A. Fischer, S. Hoogland, J. Clifford, E. Klem, L. Levina, E. H. Sargent, *Nature* **2006**, *442*, 180.